Photocatalysis Hot Paper

How to cite: *Angew. Chem. Int. Ed.* **2021**, *60*, 16085–16092
International Edition: doi.org/10.1002/anie.202104001
German Edition: doi.org/10.1002/ange.202104001

Altering Hydrogenation Pathways in Photocatalytic Nitrogen Fixation by Tuning Local Electronic Structure of Oxygen Vacancy with Dopant

Yanan Bo[+], Haiyun Wang[+], Yunxiang Lin[+], Tian Yang, Run Ye, Yu Li, Canyu Hu, Pengye Du, Yangguang Hu, Zhi Liu, Ran Long, Chao Gao, Bangjiao Ye, Li Song, Xiaojun Wu,* and Yujie Xiong**

Abstract: *To avoid the energy-consuming step of direct N≡N bond cleavage, photocatalytic N_2 fixation undergoing the associative pathways has been developed for mild-condition operation. However, it is a fundamental yet challenging task to gain comprehensive understanding on how the associative pathways (i.e., alternating vs. distal) are influenced and altered by the fine structure of catalysts, which eventually holds the key to significantly promote the practical implementation. Herein, we introduce Fe dopants into TiO_2 nanofibers to stabilize oxygen vacancies and simultaneously tune their local electronic structure. The combination of in situ characterizations with first-principles simulations reveals that the modulation of local electronic structure by Fe dopants turns the hydrogenation of N_2 from associative alternating pathway to associative distal pathway. This work provides fresh hints for rationally controlling the reaction pathways toward efficient photocatalytic nitrogen fixation.*

Introduction

The traditional industrial ammonia synthesis by the Haber-Bosch process ($N_2+3H_2\rightleftharpoons 2NH_3$) generally performs the dissociative nitrogen reduction pathway, in which the direct cleavage of N≡N triple bonds takes place prior to the addition of hydrogen atoms. To cleave the ultra-stable N≡N triple bonds (with a bond energy of 941 kJ mol^{-1}), the Haber-Bosch process requires high energy input (673–873k, 15–25 MPa).[1–3] Photocatalytic N_2 fixation ($2N_2+6H_2O\rightleftharpoons 4NH_3+3O_2$) is an attractive alternative NH_3 synthesis method to the Haber–Bosch process, because, instead of using H_2 under the harsh conditions, it employs inexhaustible solar energy and water to convert N_2 into NH_3 at ambient temperature and pressure. Essentially, such photocatalytic nitrogen reduction can be carried out under ambient condition just because it undergoes the associative pathways that no longer need to directly cleave the N≡N triple bonds, significantly reducing the required energy input. In this regard, it is a fundamental yet challenging theme to comprehensively understand how the nitrogen reduction pathways (i.e., associative alternating vs. associative distal) could be controlled and altered in a favorable way, eventually enabling efficient photocatalytic N_2 fixation.

The catalytic behavior involving reaction pathways is, to a great extent, determined by the local electronic structure of catalytic sites. In terms of controlling catalytic sites, oxygen vacancies have been extensively investigated for oxide catalysts in catalytic nitrogen reduction,[4–11] highlighting their importance as catalytic sites. For this reason, we focus on the surface oxygen vacancies using titanium dioxide (TiO_2) as a catalyst model, and aim to elucidate the mystery how their local electronic structure impacts on reaction pathways. To modulate the local electronic structure of oxygen vacancies, we decide to adopt the strategy of doping heteroatoms that has been proven as a simple and effective way toward such a purpose.[10,12–14] Another noteworthy advantage for heteroatom doping is to improve the stability of catalysts containing oxygen vacancies. In most cases, oxygen vacancies are created via annealing in a high-temperature and oxygen-

[*] Y. Bo,[+] H. Wang,[+] Dr. Y. Lin,[+] Dr. C. Hu, P. Du, Y. Hu, Prof. R. Long, Prof. C. Gao, Prof. L. Song, Prof. X. Wu, Prof. Y. Xiong
Hefei National Laboratory for Physical Sciences at the Microscale, Collaborative Innovation Center of Chemistry for Energy Materials (iChEM), School of Chemistry and Materials Science
National Synchrotron Radiation Laboratory, and
CAS Center for Excellence in Nanoscience Institution
University of Science and Technology of China
Hefei, Anhui 230026 (China)
E-mail: gaoc@ustc.edu.cn
xjwu@ustc.edu.cn
yjxiong@ustc.edu.cn

Y. Bo,[+] Prof. Y. Xiong
Institute of Energy, Hefei Comprehensive National Science Center
350 Shushanhu Rd., Hefei, Anhui 230031 (China)

T. Yang, Prof. Z. Liu
State Key Laboratory of Functional Materials for Informatics, Shanghai Institute of Microsystem and Information Technology
Chinese Academy of Sciences, Shanghai 200050 (China)

T. Yang
University of Chinese Academy of Sciences
Beijing 100049 (China)

Dr. R. Ye, Prof. B. Ye
State Key Laboratory of Particle Detection and Electronics
University of Science and Technology of China
Hefei, Anhui, 230026 (China)

Dr. Y. Li
Institute for New Energy Materials & Low-Carbon Technologies, Tianjin University of Technology
Tianjin 300384 (China)

Prof. Z. Liu
School of Physical Science and Technology, ShanghaiTech University
Shanghai 201203 (China)

[+] These authors contributed equally to this work.

Supporting information and the ORCID identification number(s) for the author(s) of this article can be found under: https://doi.org/10.1002/anie.202104001.

deficient atmosphere;[15] however, they generally tend to recombine with oxygen and disappear once exposed to air at room temperature,[16] which would severely impede our investigation on the local electronic structure of oxygen vacancies. Such a limitation can be overcome when we choose to create local oxygen vacancies by introducing heteroatoms during the synthesis process. The heteroatoms on the surface can serve as charge-compensating species to accept electrons and thus effectively stabilize oxygen vacancies. As such, heteroatom doping can provide an excellent platform for investigating the role of dopants in modulating the local electronic structure and the impact of local electronic structure adjacent to oxygen vacancy on the hydrogenation pathways in photocatalytic nitrogen fixation, which remain unexplored in the past research for oxygen vacancy-induced NRR.

Herein, we report the fabrication of iron-doped TiO_2 nanofibers via simple electrospinning toward photocatalytic fixation of N_2 to NH_3 under ambient atmosphere. The doped Fe atoms have similar radii to intrinsic Ti atoms so that the substitution of Fe dopants for Ti atoms takes place to enable localized charge compensation and thus stabilize the neighbored oxygen vacancies. The TiO_2 nanofibers with Fe-induced oxygen vacancies possess different local electronic structure from the TiO_2 nanofibers having oxygen vacancies without any doped heteroatoms, and as such, we are able to reveal the role of dopants-modulated local electronic structure in determining the reaction pathways for photocatalytic N_2 reduction. Based on in situ characterizations in combination with theoretical calculations, we reveal that tuning the local electronic structure of oxygen vacancies by doped Fe can tailor the local electron density of adsorbed N≡N, lower the energy barrier of rate-limiting step, and consequently enable the control of hydrogenation in favorable pathways. As a result, efficient and selective photocatalytic reduction of N_2 to NH_3 is achieved for the Fe-doped TiO_2 nanofibers in pure water without any sacrificial agent. This work offers a promising approach to modulate the local electronic structure toward efficient photocatalytic nitrogen fixation, as well as highlights the role of dopants-modulated local electronic structure in controlling reaction pathways.

Results and Discussion

Generally, the successful incorporation of heteroatoms as dopants highly depends on its relative radii compared to host atomic radii. If the radius of the heteroatoms is too large to enter crystal lattice, the heteroatoms would be loaded on the surface in the form of oxide.[12] When the atomic radius is similar or smaller, heteroatom may replace the host atom or be inserted into the host crystal lattice. In this work, we choose typical TiO_2 as our model catalyst and Fe as the dopant inspired by biological nitrogenase ferroprotein as well as considering the suitable radius of Fe atom compared to Ti atom.[17] To fabricate the model catalyst with high controllability, we employ electrospinning for the materials preparation in our work. Electrospinning is a universal and simple method to fabricate nanofibers at large scale with controllable morphology and flexible composition, which is economically attractive and compatible with industrial requirements for future practical application.[18] The flexible composition enlightens us to modulate electronic structure via altering pristine composition with dopants.[19,20] To this end, a series of Fe-doped TiO_2 nanofibers with different doping concentrations are prepared through a simple scalable electrospinning method (Figure 1 a) followed by annealing in air.

X-ray diffraction (XRD; Supporting Information, Figure S1) confirms that the introduction of Fe does not change the original phase or form a new phase. The diffraction patterns of all the samples match well with that of rutile phase TiO_2 (JCPDS No. 88-1172). The intensity of diffraction peaks gradually decreases and the peak position gradually shifts toward larger diffraction angles with the increase of Fe^{3+}

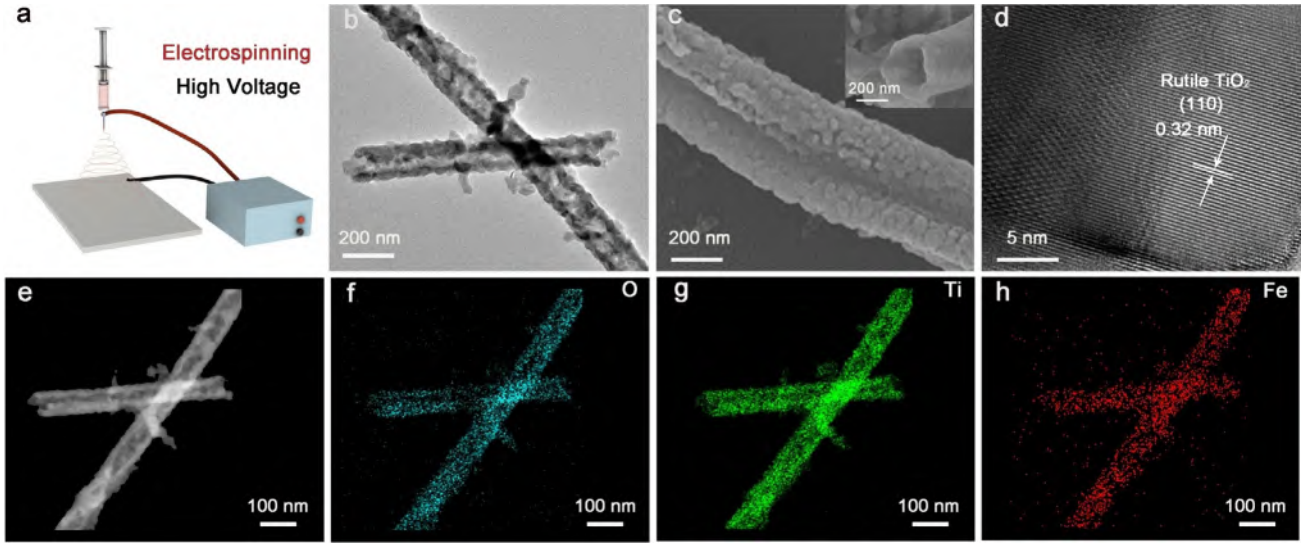

Figure 1. a) Illustration for the electrospinning setup. b) TEM, c) SEM, and d) HRTEM images of as-prepared 5-FTNFs. The inset graph in (c) shows the sectional view of as-prepared nanofibers. e) Scanning TEM image and f)–h) EDS elemental mapping.

percentage, indicating that iron has been successfully doped into TiO_2 and contracted the lattice.[21,22] Moreover, excessive doping (10%) of iron forms a new Fe_2TiO_5 phase (Figure S2). Transmission electron microcopy (TEM) image shows that one-dimensional TiO_2 nanofibers with a diameter of about 200 nm are well obtained through the electrospinning, and similar nanofibers are observed for the samples with different amounts of Fe doping (Figure S3). Upon Fe doping (5%), unique hollow structure is formed to increase surface area as observed by TEM (Figure 1b), scanning electron microscopy (SEM, Figure 1c) and Brunauer-Emmett-Teller (BET) specific surface areas (Figure S4, Table S1) on account of different ionic thermal diffusion rates between Fe^{3+} and Ti^{4+} during the annealing process.[23] To confirm the presence and distribution of Fe in the as-synthesized sample, elemental energy-dispersive X-ray spectroscopy (EDS) mapping (Figure 1d–h) is employed to characterize the sample, revealing that Fe distributes uniformly on the nanofibers. In accordance with inductively coupled plasma mass spectroscopy (ICP-MS), EDS analysis reveals that the ratio of Fe to Ti is basically conformed to feeding ratio (Table S2). According to high resolution TEM (HRTEM, Figure 1d), the as-prepared Fe-doped TiO_2 NFs are mostly exposed with (110) crystal planes. Namely, the Fe-doped TiO_2 NFs samples are noted as *x*-FTNFs ($x = 0.625$, 1.25, 2.5 and 5), where *x* refers to the molar percentage of doped Fe element.

Upon successfully obtaining the Fe-doped TiO_2 nanofibers, we are now in a position to examine the performance of FTNFs with different Fe contents as a catalyst for photocatalytic N_2 reduction. The photocatalytic experiments are performed under the irradiation of full-spectrum light in nitrogen-saturated water without any sacrificial agent, and the concentration of produced NH_4^+ is quantified by ion chromatography. As indicated in Figure 2a, the pristine TiO_2 (0-FTNFs) exhibits a low nitrogen reduction ability, while the

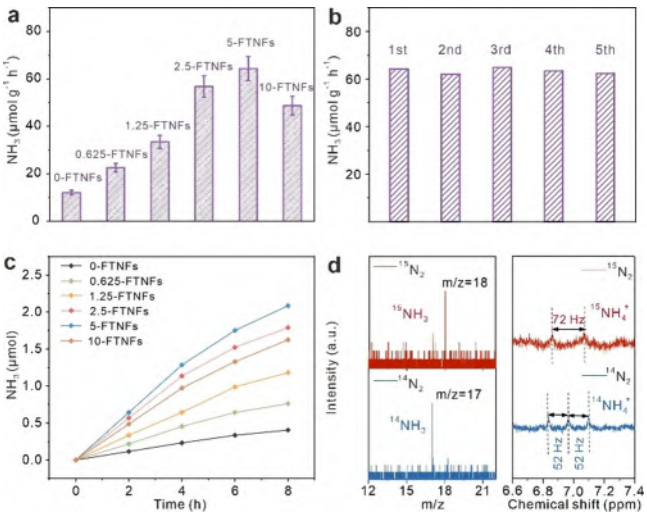

Figure 2. a) Photocatalytic NRR performance for TiO_2 nanofibers with different Fe-doping amounts. b) Photocatalytic ammonia production rates in the first 3 hours for cyclic tests of 5-FTNFs. c) Time-dependent production of NH_3 for TiO_2 nanofibers with different Fe-doping amounts. d) TOF-MS (left panel) and ^{1}H-NMR (right panel) of the products formed in different reaction atmospheres ($^{14}N_2$ or $^{15}N_2$).

NH_3 production rate for 5-FTNFs (5% Fe doping) is about 5.3 times higher than that of pristine TiO_2 NFs (12.1 vs. 64.2 $\mu mol\,g^{-1}\,h^{-1}$), suggesting that the activity for nitrogen reduction has been significantly improved by doping Fe. With the increasing doping amounts, the ammonia production rates are improved correspondingly; however, the introduction of excessive Fe (10%) leads to a decline in ammonia production rates due to the formation of a new phase of Fe_2TiO_5 (as indicated by XRD pattern and NRR performance in Figure S2 and S5). Moreover, Co-doped TiO_2 and Ni-doped TiO_2 exhibit inferior activity for photocatalytic NRR as compared with Fe-doped TiO_2, and only give slight improvement in ammonia production rates as benchmarked against pristine TiO_2 (Figure S6), suggesting the specific role of doped Fe in enhancing the photocatalytic NRR activity.

To further examine the stability of the Fe-doped TiO_2 nanofibers, the used catalysts are collected and re-dispersed in fresh water for cycling tests. After the five cycles each of which lasts 3 h, the recycled catalyst well retains the activity (Figure 2b). The X-ray photoelectron spectroscopy (XPS) characterization (Figure S7) shows that the catalyst after reaction does not undergo noticeable change in comparison with the fresh one, indicating an excellent reusability and stability of the Fe-doped TiO_2 nanofibers for photocatalytic N_2 reduction. Furthermore, the ammonia product for all the TiO_2 nanofibers with different Fe-doping amount is continuously generated over time and keeps the consistent trend (Figure 2c), demonstrating the reliability and stability of N_2 fixation. To exclude any possible NO_x and NH_3 contaminants, we have conducted control experiments in the absence of photocatalyst, without illumination or in the Ar atmosphere (Figure S8 and Table S3). No NH_3 production can be detected, providing solid evidence for the absence of any NO_x or NH_3 contaminants both in feed gas and photocatalysts. Moreover, the indophenol blue colorimetric method (Figure S9) is also adopted to confirm the actual amounts of evolved NH_3 measured by ion chromatography. We also evaluate the wavelength-dependent apparent quantum efficiency (AQE) by different monochromatic light irradiation, which matches well with the light absorption capacity of the sample (Figure S10). To further verify the nitrogen source of produced NH_3, isotope labeling photocatalytic N_2 reduction is performed by using high-purity $^{15}N_2$ as the reactant, and the product is tested by time-of-flight mass spectrometry (TOF-MS, left panel in Figure 2d) and ^{1}H nuclear magnetic resonance (^{1}H-NMR) spectroscopy (right panel in Figure 2d). In TOF-MS, the produced $^{15}NH_3$ corresponding to the $m/z = 18$ in mass spectrometry is originated from $^{15}N_2$. In ^{1}H-NMR spectroscopy, the doublet pattern with the coupling constant of $J_{N\text{-}H} = 72$ Hz corresponding to $^{15}NH_4^+$ is observed, while no triplet pattern with the coupling constant of $J_{N\text{-}H} = 52$ Hz corresponding to $^{14}NH_4^+$ can be detected. The above results confirm that the NH_3 product totally evolves from N_2 rather than any contamination.

As discussed above, the Fe doping largely promotes the activity of pristine TiO_2 nanofibers for nitrogen reduction. To elucidate the origin of this superior activity, we have to examine the influence of Fe doping on light utilization, charge separation and Fe-induced local defect structure, which are

the potential factors for altering photocatalytic performance. Our characterizations on band structures and charge separation (Figure S11–S14) indicate that doping Fe into TiO_2 lattice can promote the light utilization in visible region and facilitates the charge separation and transfer, which enables to provide abundant photogenerated electrons for N_2 reduction. However, according to the photocurrents, the improvement of light utilization and charge separation does not sufficiently enhance the photocatalytic performance to such an extent. As such, we look into the local electronic structure of active sites that could play a crucial role in determining the catalytic performance. Surface oxygen vacancies are well accepted as catalytic sites for the catalytic reduction of nitrogen. We thus closely examine the modulated local electronic structure nearby oxygen vacancy along with Fe doping. To reveal the local electronic structure, XPS measurements are conducted to analyze the valence state variation (Figure 3 and S15). The XPS spectra for 0-FTNFs show characteristic Ti $2p_{1/2}$ and $2p_{3/2}$ peaks of tetra-valent Ti^{IV} at 458.8 and 462.2 eV, respectively.[15] In comparison, these peaks for the 5-FTNFs shift to lower binding energy by about 0.24 eV (Figure 3a). In the meantime, with the increased amount of Fe dopants in TiO_2, the Fe $2p_{1/2}$ and $2p_{3/2}$ peaks of tri-valent Fe^{III} at 724.0 eV and 711.0 eV for 5-FTNFs shift to higher binding energy as compared with 0.625-FTNFs (Figure 3b).[10] Such shifts of Ti and Fe peaks in the opposite direction indicate that the local electron density of Fe decreases due to the formation of Fe—O bond while the Fe-induced oxygen vacancy increases the local electron density of Ti, which is also proven by differential charge density (Figure S16). Such lopsided local charge distribution would affect the local electron density of adsorbed N_2 molecules and thus contribute to polarizing the adsorbed N_2 molecules for better activation, as evidenced by the following DFT calculation.

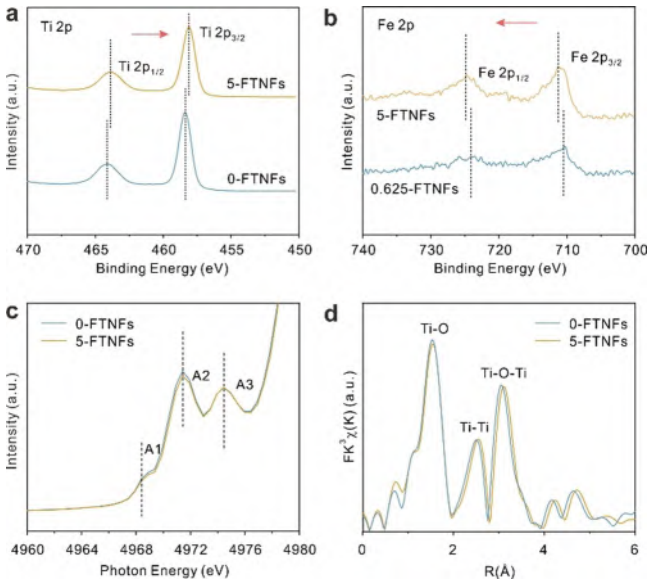

Figure 3. High-resolution a) Ti 2p and b) Fe 2p XPS spectra for 0-FTNFs and 5-FTNFs. c) Ti K-edge XANES spectra for extended edge and d) magnitude of k^3-weighted Fourier transforms of Ti K-edge EXAFS spectra for 0-FTNFs and 5-FTNFs.

X-ray absorption fine structure (XAFS) spectroscopy is further performed to probe the variation of local electronic structure caused by introducing Fe into TiO_2 lattice (Figure 3c,d and S17–S19). Generally, rutile titanium dioxide has a octahedral structure with six-fold coordination.[24,25] As shown in Figure 3c, Ti K-edge X-ray absorption near-edge structure (XANES) spectra for 0-FTNFs and 5-FTNFs possess three typical pre-edge peaks associated with the rutile phase (denoted as A1, A2, and A3), corresponding to quadruple-allowed 1s→3d transitions, dipole-allowed Ti s→p transitions with Ti 3d (t_{2g}) and Ti 3d (e_g) characters, respectively.[25] The reduced intensity of A2 peak for 5-FTNFs compared to 0-FTNFs is caused by severe Ti site distortions after Fe incorporation. The Ti site distortion can be also testified by Fourier transformed extended XAFS (EXAFS) spectra (Figure 3d), in which 5-FTNFs possess shorter equator bond length and longer apical bond length than 0-FTNFs. Essentially, such a distortion is associated with the contracted crystal lattice due to the addition of Fe, as confirmed by XRD that diffraction peaks shift to larger 2θ angles (Figure S1). Moreover, Fe K-edge XANES spectra of 5-FTNFs (Figure S18) display characteristic peaks distinguished from those of Fe foil and Fe_2O_3, excluding the exsistence of metallic Fe or Fe_2O_3 phase.[26,27] In the meantime, the addition of Fe reduces the intensity of Ti-O peak in Figure 3d, which is consistent with the smaller coordination numbers of 5-FTNFs than 0-FTNFs (4.98 vs. 6.00, Table S4). In the 5-FTNFs, the unsaturated coordinated Ti atoms are stabilized by Fe dopants through charge compensation,[10] and as such, the oxygen vacancies are stabilized to provide abundant active sites. Indeed, the concentration of oxygen vacancies in 5-FTNFs is dramatically higher than that in 0-FTNFs, as evidenced by positron annihilation spectrometry (Figure S20 and Table S5). All these evidences indicate that heteroatom Fe has been successfully incorporated into TiO_2 lattice and simultaneously modulated the local electronic structure nearby oxygen vacancies.

To further understand the role of tuning local electronic structure for nitrogen reduction reaction, various spectral characterizations are performed to examine the interactions of catalyst with N_2 molecules. The electron paramagnetic resonance (EPR) spectrum of 5-FTNFs under the He atmosphere shows a clear signal near $g = 2.003$ (Figure 4a), indicating the presence of abundant oxygen vacancies although the preparation process involves annealing in air. In contrast, no obvious signal of oxygen vacancies is observed in the EPR spectra of 0-FTNFs prepared via the same air-annealing (Figure S21a) as the annealing in air generally removes the oxygen vacancies. For this reason, the oxygen vacancies in 0-FTNFs appear after post annealing in anoxic Ar atmosphere (denoted as 0-FTNFs-Ar). This indicates that the Fe dopants are capable of inducing the formation of abundant oxygen vacancies no matter whether the post annealing is performed in air. The 0-FTNFs-Ar with substantially more oxygen vacancies exhibits an inferior NRR activity in contrast to 5-FTNFs (Figure S21b–d, Table S6), suggesting that the Fe dopants play an important role in

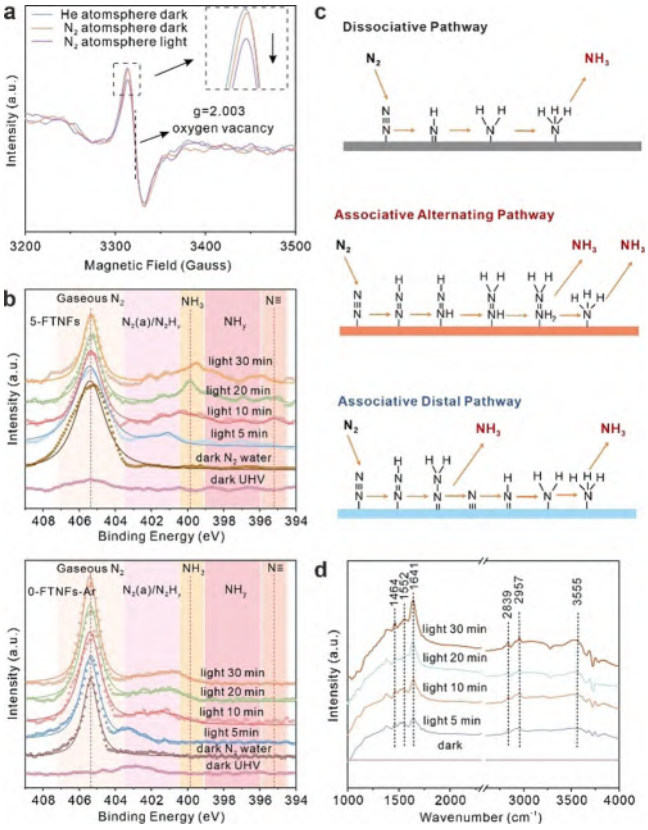

Figure 4. a) EPR spectra of 5-NFTFs in the conditions of He atmosphere under dark, N_2 atmosphere under dark and N_2 atmosphere under light irradiation, respectively. b) In situ NAP-XPS spectra of 5-FTNFs and 0-FTNFs-Ar collected in the conditions of ultrahigh vacuum under dark, N_2 atmosphere under dark and N_2 atmosphere under light irradiation, respectively. c) Pathway for N_2 reduction on heterogeneous catalysts: dissociative pathway (top), associative alternating pathway (middle) and associative distal pathway (bottom). d) In situ DRIFT spectra of 5-NFTFs collected in N_2 atmosphere under dark and irradiation.

facilitating the NRR process. The role of Fe dopants in promoting the formation of oxygen vacancies is further confirmed by DFT calculations, which indicate that the introduction of Fe into TiO_2 can reduce the formation energy for oxygen vacancy (−3.56 eV for Fe-doped TiO_2 vs. −1.83 eV for pristine TiO_2, Table S7). Essentially, such Fe-induced oxygen vacancies are formed through the replacement of Ti^{IV} by Fe^{III}, and the oxygen vacancies exist stably because Fe^{III} acts as an electron compensation.

We further examine the interaction of catalyst with N_2 molecules by purging N_2 into the testing tube. The presence of N_2 reduces the signal intensity of oxygen vacancies, illustrating that oxygen vacancies could interact with N_2. Upon illumination, the signal intensity of oxygen vacancies further declines, indicating that the oxygen vacancies are involved in N_2 reduction.[28,29] To reveal the relationship between oxygen vacancy and NRR activity, we compare the oxygen vacancy contents of 0-FTNFs-Ar and 5-FTNFs. The raletive oxygen vacancy contents are quantitatively analyzed by O 1s XPS spectra (Figure S21b and c), in which the oxygen vacancy content for 0-FTNFs-Ar is nearly double that of 5-FTNFs.[7] However, 0-FTNFs-Ar with much more oxygen vacancies exhibits an inferior NRR activity in contrast to 5-FTNFs (Figure S21d), suggesting that the Fe dopants play an important role in facilitating the NRR process. Taken together, the EPR characterizations demonstrate that the doped Fe can induce the formation of oxygen vacancies, which bring about abundant active sites for N_2 adsorption involved in the NRR process. Beyond that, the doped Fe can exert significant influence on NRR process contributing to a higher activity even with lower oxygen vacancy content, as discussed in the following section.

During the NRR process, the N_2 adsorption is followed by chemical reactions. N_2 is a symmetric nonpolar molecule so that its binding with a certain atom of catalyst surface will lead to the redistribution of spatial charge and weakening of N≡N triple bond. In this case, the local electronic structure nearby active sites would largely influence the adsorption and polarization of N_2 molecule and thus alter the reaction pathways for N_2 hydrogenation. To reveal such impact on the reaction pathways for N_2 hydrogenation, in situ near ambient pressure X-ray photoelectron spectroscopy (NAP-XPS) is performed for the reaction system using 5-FTNFs as a catalyst in reference to 0-FTNFs-Ar. Both the catalysts contain oxygen vacancies but only 5-FTNFs is incorporated with Fe dopants. We collect the time-dependent NAP-XPS spectra for N 1s (Figure 4b), which gives the information of N-containing intermediates. Gaseous nitrogen exhibits higher binding energy for its ultra-stable triple bond (941.7 kJ mol^{-1}) contrasting to double bond and single bond. In general, the binding energies of N-containing species decline in the sequence of gaseous N_2 > chemical absorbed N_2 > N_2H_x ($x = 1$–4) > NH_y ($y = 1$–3).[30] More specifically, along with the hydrogenation process, the binding energies of N-containing species increase, that is, N≡ < -NH- < -NH_2 < NH_3. Our time-dependent NAP-XPS shows no obvious signal under the ultrahigh vacuum (UHV), and then the signal of gaseous N_2 appears at 405.3 eV and exists concomitantly during the whole reaction after high-purity N_2 is introduced into the analysis chamber. In the case of 5-FTNFs (Figure 4b, top), after illumination of 5 min, a broader band around 402.0 eV ascribed to adsorbed N_2 molecule [N_2(a)] shows up clearly and can be resolved into two peaks, revealing the states of two different nitrogen atoms in a discrepant chemical environment.[31] Along with the illumination of 10–30 min, the band of absorbed N_2 molecule varies between 400–402 eV, suggesting that the adsorbed N_2 molecule has been hydrogenated to N_2H_y ($y = 1$ or 2).[32] As hydrogenation continuously proceeds, the signal of N=N is gradually weakened and two peaks emerge at 395.3 and 397–399 eV that are attributed to N≡ and NH_y ($y = 1$ or 2), respectively.[33] This indicates that the N=N species evolves into N≡ and NH_y during the subsequent reaction steps. Apparently, no signal for N≡ is observed at the initial stage of the reaction, excluding the possibility of dissociative pathway. Furthermore, the observation of N≡ and NH_y intermediates during the reaction confirms that the 5-FTNFs takes the associative distal pathway for N_2 reduction as illustrated in Figure 4c.

As a comparison, the 0-FTNFs-Ar catalyst contains oxygen vacancies but no Fe dopants. Upon illumination, the

signal for adsorbed N_2 appears at 402.8 eV (Figure 4b, bottom). As the illumination prolongs, the signal for N_2H_y ($y=1$–4) species emerges at 401–402 eV and eventually evolves into NH_3 at 399.8 eV. During the nitrogen reduction reaction on 0-FTNFS-Ar, the peaks for N≡ (395.3) and NH_y ($y=1$ or 2, 397–399 eV) fragments do not emerge throughout the process. This manifests that the 0-FTNFs-Ar takes the associative alternating pathway for N_2 reduction (Figure 4c). The NAP-XPS results here provide a direct evidence that the addition of Fe dopants in TiO_2 can turn the hydrogenation of N_2 from the associative alternating pathway to associative distal pathway.

To verify the reaction mechanism upon N_2 reduction, in situ diffuse reflectance infrared Fourier-transform spectroscopy (DRIFTS) is also employed to monitor the intermediates during the photocatalytic N_2 reduction process. The in situ DRIFT spectra of 5-FTNFs (Figure 4d) show that the signal of N-bearing intermediates arises and is gradually boosted with time under illumination. The broad band at 3555 cm^{-1} corresponds to the ν(N-H) stretching mode, while the sharp band at 1641 cm^{-1} can be assigned to the σ(N-H) bending mode. Furthermore, the weak bands at 1464 and 2839 cm^{-1} are attributed to the characteristic adsorption of NH_4^+, while the bands at 1552 and 2957 cm^{-1} are ascribed to the characteristic absorption of NH_3 molecule.[6,29] These signals of N intermediates are in good accordance with in situ NAP-XPS characterization, providing a convictive proof for the reaction pathway.

To elucidate how the tuning of local electronic structure by Fe dopants impacts on the reaction pathway of N_2 hydrogenation in NRR, density functional theory (DFT) calculations are further performed to examine the evolution of N_2 molecule on catalyst surface. According to EXAFS results, we first calculate various possible structures and select the most stable structure as a slab model as illustrated in Figure S22. For ease of description, we denote the active sites of Fe-free 0-FTNFs-Ar and Fe-doped 5-FTNFs samples as Ti-Ovs-Ti and Fe-Ovs-Ti sites, respectively. In both cases, N_2 adsorption takes an end-on configuration. However, the adsorption in Fe-Ovs-Ti takes place at the Fe sites nearby oxygen vacancies (Figure S23), while the adsorption sites in Ti-Ovs-Ti are the Ti atoms at the oxygen vacancies (Figure S24). We then simulate the Gibbs free energies of both the associative distal pathway and associative alternating pathway at two different sites (i.e., Ti-Ovs-Ti and Fe-Ovs-Ti) (Figure 5, S25and S26). In the case of Ti-Ovs-Ti sites, the first hydrogenation step of NRR ($N_2+H^++e^-\rightleftharpoons N_2H^*$) proceeds easily with a downhill Gibbs free energy change (ΔG) of −0.357 eV, but the next hydrogenation step has an uphill energy barrier for the formation of both NHNH* (0.251 eV) in the associative alternating pathway and NH_2* (0.431 eV) in the associative distal pathway (Table S8). Considering the lower uphill energy barrier, the N_2 molecule at the Ti-Ovs-Ti site prefers to be hydrogenated in the associative alternating pathway for N_2 reduction. In terms of Fe-Ovs-Ti sites, the first hydrogenation step for the formation of N_2H* has an uphill

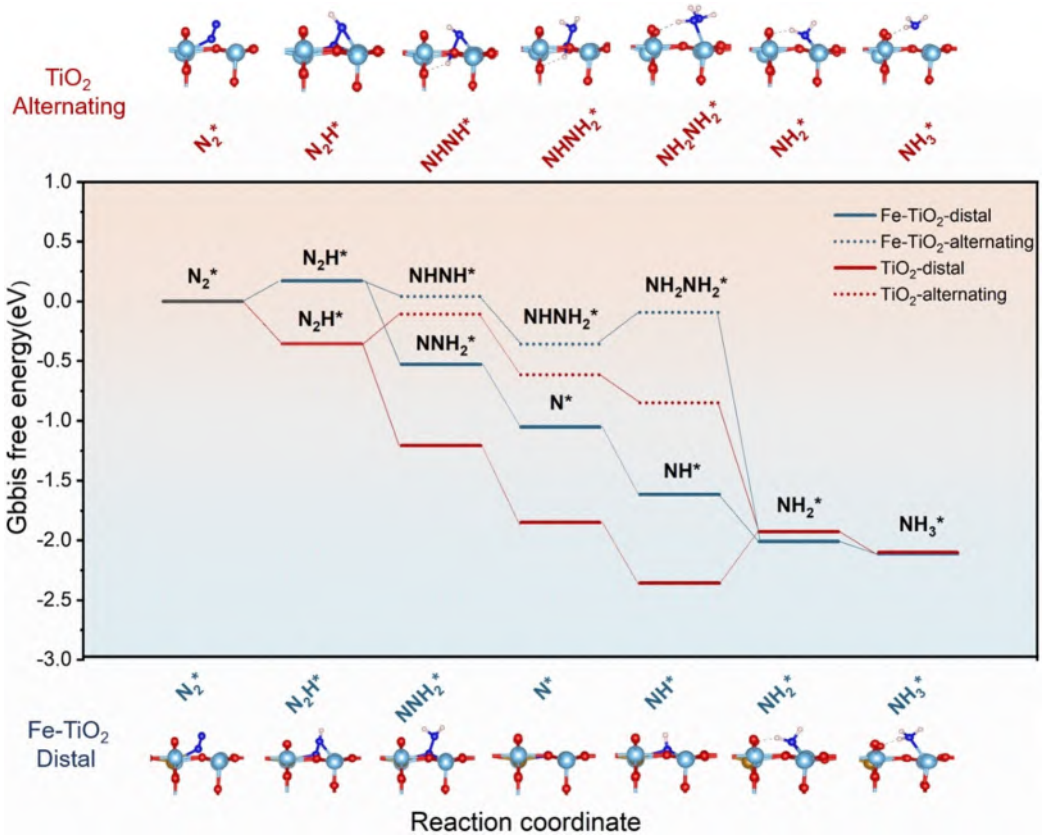

Figure 5. Calculated Gibbs free energy profiles of NRR process at Ti-Ovs-Ti (red) and Fe-Ovs-Ti sites (blue) with associative distal and associative alternating pathways and the corresponding optimized geometric structure of intermediates adsorbed on the substrate.

energy barrier of 0.171 eV. Afterwards, the subsequent hydrogenation process becomes much easier with gradual downhill Gibbs free energy in the associative distal pathway. In comparison, there is an uphill energy barrier for the formation of NH_2NH_2* in the associative alternating pathway.

Therefore, the N_2 adsorbed at the Ti-Ovs-Fe site tends to be hydrogenated in the associative distal pathway. Indeed, we have detected the corresponding N-containing intermediates for Fe-doped 5-FTNFs (Ti-Ovs-Fe sites) and for Fe-free 0-FTNFs-Ar (Ti-Ovs-Ti sites) during the reaction in above in situ characterizations, which provides a solid evidence to confirm the calculation results. Furthermore, the limiting-potential of NRR at the Ti-Ovs-Fe sites ($N_2 + H^+ + e^- \rightleftharpoons N_2H$*, 0.171 eV) is substantially lower than that of Ti-OVs-Ti sites ($NNH + H^+ + e^- \rightleftharpoons NNH_2$*, 0.251 eV). This implies that the Fe-doped catalyst can proceed hydrogenation more easily enhancing the photocatalytic activity in NRR.

Then a fundamental question naturally arises what factor alters the hydrogenation pathways in NRR. The schematic illustration for reaction pathways (Figure 4c) gives us a clue. In the associative distal pathway, the hydrogenation first takes place on one N atom to form one NH_3, and then the hydrogenation proceeds on another N atom. In sharp contrast, the hydrogenation in the associative alternating pathway should proceed on both two N atoms simultaneously. Thus the key to altering the reaction pathways is to differentiate the two N atoms in a N_2 molecule. To look into the difference of two N atoms at the Fe-Ovs-Ti site, we acquire the differential charge diagram (Figure S27) that can reflect the polarization of adsorbed N_2 molecule, which shows that the electrons can be preferentially accumulated on the N atom bonded with Fe site. Such an imbalanced charge distribution differentiates the two N atoms of adsorbed N_2, initiating the associative distal pathway at the Fe-Ovs-Ti site. Taken together, the computational studies and in situ characterizations highlight that the introduction of Fe dopants into catalyst is an efficient approach to create active sites and modulate local electronic structure, which dramatically alter the reaction pathways and substantially enhance the efficiency for N_2-to-NH_3 conversion.

Conclusion

We have developed a doping strategy to modulate the local electronic structure of surface vacancy for controlling the photocatalytic nitrogen fixation in a favorable hydrogenation pathway. We have revealed that the doped Fe atoms in TiO_2 nanofibers can modulate the local electronic structure nearby oxygen vacancy and act as binding sites. Such an effect in turn facilitates the adsorption and polarization of N_2, lowers the energy barrier of rate-limiting step for nitrogen reduction, and consequently alters the hydrogenation of N_2 from the associative alternating pathway to a more favorable associative distal pathway, thus contributing to improved performance for NH_3 evolution in photocatalytic nitrogen fixation. This work sheds a light on the rational design of catalytic sites toward efficient photocatalytic nitrogen fixation through modulating local electronic structure and provides comprehensive understanding on how the dopants-modulated local electronic structure could alter reaction pathways.

Acknowledgements

This work was supported by the National Key R&D Program of China (2017YFA0207301), NSFC (21725102, 91961106, 91963108, 21703220, 11875248), CAS Key Research Program of Frontier Sciences (QYZDB-SSW-SLH018), CAS Interdisciplinary Innovation Team, DNL Cooperation Fund, CAS (DNL201922), and Youth Innovation Promotion Association CAS. XAFS measurements were performed at the beamline BL14W1 of the Shanghai Synchrotron Radiation Facility (SSRF), China. A portion of this work was performed on the Steady High Magnetic Field Facilities, High Magnetic Field Laboratory, CAS. In situ DRIFTS was collected at the Infrared Spectroscopy and Microspectroscopy Endstation (BL01B), and TOF-MS measurements were performed on synchrotron radiation ultraviolet photoionization mass spectroscopy (SR-PIMS, BL04B) in the National Synchrotron Radiation Laboratory (NSRL) in Hefei, China. We are thankful for the support from the USTC Center for Micro- and Nanoscale Research and Fabrication.

Conflict of interest

The authors declare no conflict of interest.

Keywords: active sites · hydrogenation pathway · local electronic structure · oxygen vacancy · photocatalytic nitrogen fixation

[1] J. W. Erisman, M. A. Sutton, J. Galloway, Z. Klimont, W. Winiwarter, *Nat. Geosci.* **2008**, *1*, 636 – 639.
[2] X. Xue, R. Chen, C. Yan, P. Zhao, Y. Hu, W. Zhang, S. Yang, Z. Jin, *Nano Res.* **2019**, *12*, 1229 – 1249.
[3] C. Chen, X. Zhu, X. Wen, Y. Zhou, L. Zhou, H. Li, L. Tao, Q. Li, S. Du, T. Liu, D. Yan, C. Xie, Y. Zou, Y. Wang, R. Chen, J. Huo, Y. Li, J. Cheng, H. Su, X. Zhao, W. Cheng, Q. Liu, H. Lin, J. Luo, J. Chen, M. Dong, K. Cheng, C. Li, S. Wang, *Nat. Chem.* **2020**, *12*, 717 – 724.
[4] N. Zhang, A. Jalil, D. Wu, S. Chen, Y. Liu, C. Gao, W. Ye, Z. Qi, H. Ju, C. Wang, X. Wu, L. Song, J. Zhu, Y. Xiong, *J. Am. Chem. Soc.* **2018**, *140*, 9434 – 9443.
[5] C. Lv, Y. Qian, C. Yan, Y. Ding, Y. Liu, G. Chen, G. Yu, *Angew. Chem. Int. Ed.* **2018**, *57*, 10246 – 10250; *Angew. Chem.* **2018**, *130*, 10403 – 10407.
[6] S. Wang, X. Hai, X. Ding, K. Chang, Y. Xiang, X. Meng, Z. Yang, H. Chen, J. Ye, *Adv. Mater.* **2017**, *29*, 1701774.
[7] C. Li, T. Wang, Z. J. Zhao, W. Yang, J. F. Li, A. Li, Z. Yang, G. A. Ozin, J. Gong, *Angew. Chem. Int. Ed.* **2018**, *57*, 5278 – 5282; *Angew. Chem.* **2018**, *130*, 5376 – 5380.
[8] H. Wang, D. Yong, S. Chen, S. Jiang, X. Zhang, W. Shao, Q. Zhang, W. Yan, B. Pan, Y. Xie, *J. Am. Chem. Soc.* **2018**, *140*, 1760 – 1766.
[9] S. Bai, N. Zhang, C. Gao, Y. Xiong, *Nano Energy* **2018**, *53*, 296 – 336.
[10] Y. Tong, H. Guo, D. Liu, X. Yan, P. Su, J. Liang, S. Zhou, J. Liu, G. Q. Lu, S. X. Dou, *Angew. Chem. Int. Ed.* **2020**, *59*, 7356 – 7361; *Angew. Chem.* **2020**, *132*, 7426 – 7431.

[11] J. Qian, S. Zhao, W. Dang, Y. Liao, W. Zhang, H. Wang, L. Lv, L. Luo, H.-Y. Jiang, J. Tang, *Adv. Sustainable Syst.* **2021**, *5*, 2000282.
[12] Y. Zhou, F. Che, M. Liu, C. Zou, Z. Liang, P. De Luna, H. Yuan, J. Li, Z. Wang, H. Xie, H. Li, P. Chen, E. Bladt, R. Quintero-Bermudez, T.-K. Sham, S. Bals, J. Hofkens, D. Sinton, G. Chen, E. H. Sargent, *Nat. Chem.* **2018**, *10*, 974 – 980.
[13] J. Zhang, X. Tian, M. Liu, H. Guo, J. Zhou, Q. Fang, Z. Liu, Q. Wu, J. Lou, *J. Am. Chem. Soc.* **2019**, *141*, 19269 – 19275.
[14] T. Wu, X. Zhu, Z. Xing, S. Mou, C. Li, Y. Qiao, Q. Liu, Y. Luo, X. Shi, Y. Zhang, X. Sun, *Angew. Chem. Int. Ed.* **2019**, *58*, 18449 – 18453; *Angew. Chem.* **2019**, *131*, 18620 – 18624.
[15] J. Yang, Y. Guo, R. Jiang, F. Qin, H. Zhang, W. Lu, J. Wang, J. C. Yu, *J. Am. Chem. Soc.* **2018**, *140*, 8497 – 8508.
[16] Q. Wu, Q. Zheng, R. van de Krol, *J. Phys. Chem. C* **2012**, *116*, 7219 – 7226.
[17] D. Sippel, M. Rohde, J. Netzer, C. Trncik, J. Gies, K. Grunau, I. Djurdjevic, L. Decamps, S. L. A. Andrade, O. Einsle, *Science* **2018**, *359*, 1484 – 1489.
[18] L. Persano, A. Camposeo, C. Tekmen, D. Pisignano, *Macromol. Mater. Eng.* **2013**, *298*, 504 – 520.
[19] J. Xue, T. Wu, Y. Dai, Y. Xia, *Chem. Rev.* **2019**, *119*, 5298 – 5415.
[20] D. Joly, J.-W. Jung, I.-D. Kim, R. Demadrille, *J. Mater. Chem. C* **2016**, *4*, 10173 – 10197.
[21] J. Yang, H. Bai, Y. Guo, H. Zhang, R. Jiang, B. Yang, J. Wang, J. C. Yu, *Angew. Chem. Int. Ed.* **2021**, *60*, 927 – 936; *Angew. Chem.* **2021**, *133*, 940 – 949.
[22] H. He, D. Sun, Q. Zhang, F. Fu, Y. Tang, J. Guo, M. Shao, H. Wang, *ACS Appl. Mater. Interfaces* **2017**, *9*, 6093 – 6103.
[23] C. Lv, C. Yan, G. Chen, Y. Ding, J. Sun, Y. Zhou, G. Yu, *Angew. Chem. Int. Ed.* **2018**, *57*, 6073 – 6076; *Angew. Chem.* **2018**, *130*, 6181 – 6184.
[24] Q. Wu, R. van de Krol, *J. Am. Chem. Soc.* **2012**, *134*, 9369 – 9375.
[25] N. Jiang, D. Su, J. C. H. Spence, *Phys. Rev. B* **2007**, *76*, 214117.
[26] Z. Zhang, Q. Wu, G. Johnson, Y. Ye, X. Li, N. Li, M. Cui, J. D. Lee, C. Liu, S. Zhao, S. Li, A. Orlov, C. B. Murray, X. Zhang, T. B. Gunnoe, D. Su, S. Zhang, *J. Am. Chem. Soc.* **2019**, *141*, 16548 – 16552.
[27] M. Açıkgöz, P. Gnutek, C. Rudowicz, *Chem. Phys. Lett.* **2012**, *524*, 49 – 55.
[28] Y. Zhao, Y. Zhao, R. Shi, B. Wang, G. I. N. Waterhouse, L. Z. Wu, C. H. Tung, T. Zhang, *Adv. Mater.* **2019**, *31*, 1806482.
[29] H. Hirakawa, M. Hashimoto, Y. Shiraishi, T. Hirai, *J. Am. Chem. Soc.* **2017**, *139*, 10929 – 10936.
[30] C. Hu, X. Chen, J. Jin, Y. Han, S. Chen, H. Ju, J. Cai, Y. Qiu, C. Gao, C. Wang, Z. Qi, R. Long, L. Song, Z. Liu, Y. Xiong, *J. Am. Chem. Soc.* **2019**, *141*, 7807 – 7814.
[31] M. L. Wagner, L. D. Schmidt, *Surf. Sci. Lett.* **1991**, *257*, A565.
[32] J. Zheng, Y. Lyu, M. Qiao, J. P. Veder, R. D. Marco, J. Bradley, R. Wang, Y. Li, A. Huang, S. P. Jiang, S. Wang, *Angew. Chem. Int. Ed.* **2019**, *58*, 18604 – 18609; *Angew. Chem.* **2019**, *131*, 18777 – 18782.
[33] J. L. Bischoff, F. Lutz, D. Bolmont, L. Kubler, *Surf. Sci.* **1991**, *251*, 170 – 174.

Manuscript received: March 21, 2021
Revised manuscript received: April 27, 2021
Accepted manuscript online: May 7, 2021
Version of record online: June 14, 2021

